Inorganic Chemistry

pubs.acs.org/IC

Article

Mn-Doped Zn Metal−Organic Framework-Derived Porous N-Doped Carbon Composite as a High-Performance Nonprecious Electrocatalyst for Oxygen Reduction and Aqueous/Flexible Zinc−Air Batteries

Lixia Wang, Meijiao Xu, Huatong Li, Zhiyang Huang, Lei Wang,* Tayirjan Taylor Isimjan,* and Xiulin Yang*

Cite This: *Inorg. Chem.* 2023, 62, 13284−13292

Read Online

ACCESS | Metrics & More | Article Recommendations | Supporting Information

ABSTRACT: Developing low-cost, efficient, and stable oxygen reduction reaction (ORR) electrocatalysts is crucial for the commercialization of energy conversion devices such as metal−air batteries. In this study, we report a Mn-doped Zn metal−organic framework-derived porous N-doped carbon composite (30-ZnMn-NC) as a high-performance ORR catalyst. 30-ZnMn-NC exhibits excellent electrocatalytic activity, demonstrating a kinetic current density of 9.58 mA cm^{-2} (0.8 V) and a half-wave potential of 0.83 V, surpassing the benchmark Pt/C and most of the recently reported non-noble metal-based catalysts. Moreover, the assembled zinc−air battery with 30-ZnMn-NC demonstrates high peak power densities of 207 and 66.3 mW cm^{-2} in liquid and flexible batteries, respectively, highlighting its potential for practical applications. The excellent electrocatalytic activity of 30-ZnMn-NC is attributed to its unique porous structure, the strong electronic interaction between metal Zn/Mn and adjacent N-doped carbon, as well as the bimetallic Mn/Zn−N active sites, which synergistically promote faster reaction kinetics. This work offers a controllable design strategy for efficient electrocatalysts with porous structures and bimetallic active sites, which can significantly enhance the performance of energy conversion devices.

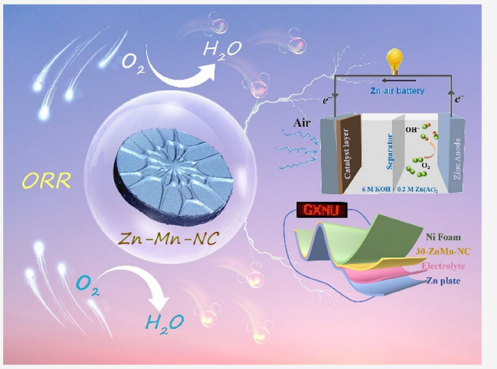

INTRODUCTION

Extensive research has been conducted on energy conversion and storage technologies, including fuel cells and metal−air batteries, with the aim of addressing the overconsumption of nonrenewable energy sources and the resulting environmental degradation.[1] Zinc−air batteries (ZABs) have the potential to serve as a renewable energy storage and conversion technology due to the high theoretical energy density (1084 Wh kg^{-1}), economic feasibility, reliability, and environmental friendliness.[2,3] However, the slow kinetics of the oxygen reduction reaction (ORR), which is the primary process of ZAB discharge, severely restricts their advancement because of the influence of the four-electron transfer pathway.[4−6] While Pt-based materials have been extensively studied as highly efficient electrocatalysts for oxygen reduction, their scarcity, low stability, and high cost inevitably limit their application in sustainable energy conversion systems.[7,8] Hence, the development of profitable and highly efficient nonprecious metal-based electrocatalysts is of utmost importance in advancing the performance of ZABs.

Metal−organic frameworks (MOFs), constructed through the self-assembly of metal ions and organic linkers, are widely recognized as excellent materials for constructing porous frameworks and are well-established in catalytic and energy storage conversion devices.[9] When zinc is used as the metal source in MOFs, it is highly volatile during high-temperature processing, ascribed to its low melting and boiling points, resulting in a porous structure of the composite that provides channels for the rapid transport of substances during the ORR process.[10] Doping N can significantly affect the charge distribution of carbon atoms, leading to increased spin density, thus stimulating the atomic activity and improving the electrical conductivity and catalytic activity of catalysts.[11−13] Transition-metal N-doped carbon composites have garnered significant interest in the domain of electrocatalysis by virtue of their exceptional electrical conductivity and excellent corrosion resistance.[14−18] Among them, Fe−N−C catalysts explicit the best ORR activity due to their efficient atom utilization.[19] Despite this advantage, it is important to note that the Fenton

Received: May 11, 2023
Published: August 5, 2023

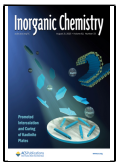

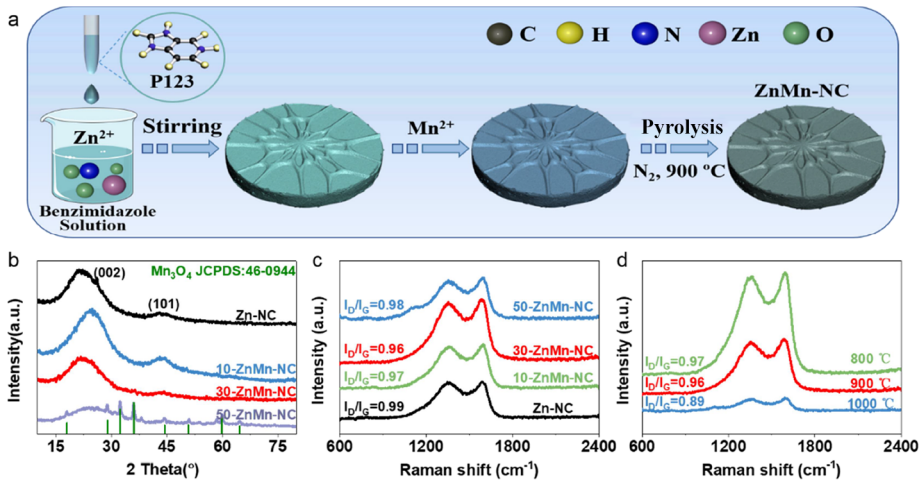

Figure 1. (a) Schematic illustration of the synthesis procedure. (b) XRD pattern of *x*-ZnMn-NC. (c) Raman spectra of *x*-ZnMn-NC samples. (d) Raman spectra of 30-ZnMn-NC (T).

reaction is prone to occur between iron ions and hydrogen peroxide (H_2O_2), and the resulting hydroxyl (OH) radicals can lead to low catalytic efficiency and poor stability of materials.[20] Consequently, Fe-free catalysts (such as Ni, Co, Mn, and Cu) have received considerable attention from researchers.[21] Currently, Mn-based ORR catalysts have been extensively studied as a substitute for Pt-based catalysts in Zn−air batteries.[22] For instance, Sun et al. developed Mn-NC/CNT catalysts that demonstrated satisfactory ORR performance with an onset potential (E_{onset}) of 0.91 V and a half-wave potential ($E_{1/2}$) of 0.83 V (vs RHE).[23] Moreover, Hu et al. reported that N−C-wrapped Mn_3O_4 nanoparticles exhibited superior ORR activity, ultralong durability, and methanol tolerance in alkaline media, surpassing that of commercial Pt/C.[24] Overall, Mn-based ORR catalysts have both advantages and disadvantages compared to Pt-based catalysts. While they are cheaper, highly active, and stable, they also have limitations such as poor selectivity, surface oxidation, and performance degradation under certain conditions.[25] Additional investigation is required to gain a comprehensive understanding of the underlying mechanism of ORR catalysis by Mn-based catalysts and to optimize their performance for practical applications in fuel cells. A recent study has revealed that the $ZnMn_2O_4$/carbon composite exhibits excellent catalytic activity for ORR in an aqueous alkaline medium. The composite exhibited an impressive onset potential of 0.90 V (vs RHE). Additionally, the recycled $ZnMn_2O_4$ demonstrated a comparable performance (around 1.0 V) to its chemically synthesized counterpart, with a specific capacity of 210 mA h g_{Zn}^{-1} under a constant current discharge of 15 mA cm^{-2}.[26] These findings suggest the possibility of further improving the ZnMn-based ORR catalyst using the MOF strategy, which has not been reported thus far.

Building on the aforementioned discovery, porous cake-like ZnMn-NC composites were obtained by loading Mn into Zn-MOF and subjecting it to high-temperature pyrolysis. The resulting ZnMn-NC catalyst exhibited abundant porous structures with a higher specific surface area and an increased number of active sites, resulting in an enhanced ORR activity. The obtained 30-ZnMn-NC displayed an $E_{1/2}$ value of 0.83 V and an E_{onset} value of 0.95 V in an alkaline electrolyte, which are comparable to that of commercial Pt/C (0.84 V, 1.01 V). The ZAB based on 30-ZnMn-NC demonstrated a peak power density of 207 mW cm^{-2} and a low voltage decay rate during 85 h of charge/discharge operation, indicating its great potential for practical energy conversion applications.

RESULTS AND DISCUSSION

Synthesis and Structural Characterization. Figure 1a illustrates the synthetic process of ZnMn-NC. First, the mixture of $Zn(NO_3)_2{\cdot}6H_2O$, BIM, and $MnSO_4{\cdot}H_2O$ is stirred in a solution composed of ethanol and deionized water in two steps. Subsequently, the cake-like ZnMn-NCs were fabricated by pyrolyzing the precursor at 900 °C. XRD was employed to verify the phase composition and crystallinity of the synthesized electrocatalyst. The XRD pattern (Figure S2) shows that the crystalline phase of 30-ZnMn-MOF is comparable to that of Zn-MOF.[27] Furthermore, TEM, the corresponding elemental mappings, and EDS spectra confirmed that Mn has been successfully doped into Zn-MOF (Figures S3−4). In Figure 1b, it can be observed that the prepared Zn-NC, 10-ZnMn-NC, and 30-ZnMn-NC had two distinct diffraction peaks at 25° and 43°, which can be attributed to the crystal planes (002) and (101) of graphitic carbon.[28] However, due to the low crystallinity and partially graphitized structure, the characteristic diffraction peaks of Mn and Zn species were not observed in this composite. Notably, the XRD patterns of 50-ZnMn-NC show several diffraction peaks at 29°, 31°, and 39° that matched the characteristic diffraction peak of Mn_3O_4 (JCPDS: 46-0944).[29] This provides strong evidence that 50-ZnMn-NC is primarily composed of Mn_3O_4. The Raman spectrum exhibited two signal peaks at 1355 and 1594 cm^{-1} (Figure 1c), which reflected the defects and disorder of sp^3 carbon in the material (D band) and the graphitization degree of sp^2 hybrid carbon in the graphite structure (G band), respectively. The graphitic carbon favors electrical conductivity, while defective carbon provides abundant active sites.[30] The value of I_D/I_G for 30-ZnMn-NC was 0.96, which was almost the same as that of Zn-NC (0.99), 10-ZnMn-NC (0.97), and 50-ZnMn-NC (0.98), suggesting that the inclusion of Mn had a minimal effect on the degree of graphitization. In Figure 1d, I_D/I_G decreased gradually with increasing temperature (0.97, 0.96, and 0.89 at 800, 900, and 1000 °C, respectively), validating that higher temperature could result in the reduction of defective carbon and increase in the graphitization degree. Importantly, an appropriate

https://doi.org/10.1021/acs.inorgchem.3c01536
Inorg. Chem. 2023, 62, 13284−13292

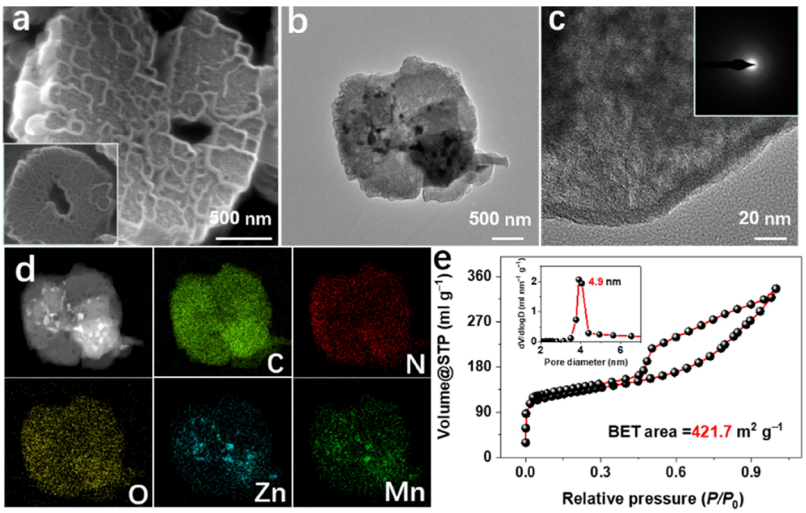

Figure 2. (a) SEM image of 30-ZnMn-NC with the (inset) SEM image of 30-ZnMn-MOF. (b) TEM image, (c) HR-TEM image, (d) HAADF-STEM images, and the corresponding elemental mappings, and (e) N_2 adsorption/desorption isotherms and the corresponding pore size distribution (inset) for 30-ZnMn-NC.

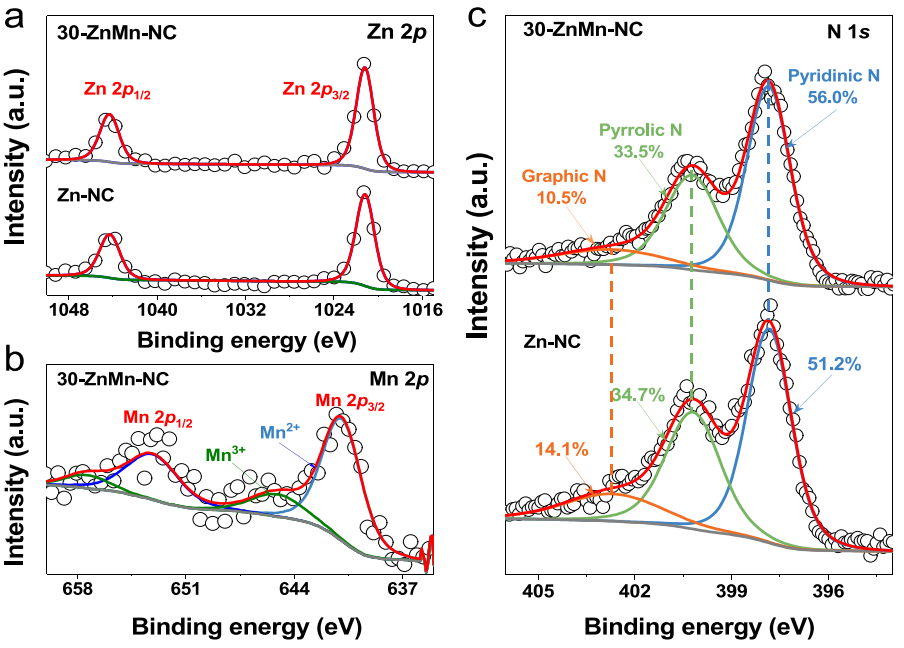

Figure 3. High-resolution XPS spectra of (a) Zn 2p, (b) Mn 2p, and (c) N 1s in Zn-NC and 30-ZnMn-NC.

degree of carbon defects and graphitization is crucial for enhancing the ORR performance.[31]

Microstructure Analysis. The micro-morphological characteristics of the 30-ZnMn-MOF precursor and 30-ZnMn-NC catalyst were analyzed using scanning electron microscopy (SEM) and TEM. The 30-ZnMn-MOF precursor presented a cake-like structure with surface wrinkles (Figure 2a), while the morphology of 30-ZnMn-NC obtained by high-temperature pyrolysis maintained its inherent framework structure without collapsing. The existence of the pore structure was clearly observed in Figure 2b, mainly attributed to the volatilization of Zn atoms during the pyrolysis process. The high-resolution TEM image (HR-TEM) and the selected-area electron diffraction (SAED) image (Figure 2c) revealed the low crystallinity and high dispersion of the metal composites, which were mutually corroborated by the XRD analysis results. Furthermore, high-angle annular dark-field STEM (HAADF-STEM) confirmed the porous cake-like structure of 30-ZnMn-NC, and the corresponding elemental mapping disclosed the even distribution of C, O, N, Zn, and Mn throughout the 30-ZnMn-NC structure (Figure 2d). The Zn and Mn contents of all samples were measured using inductively coupled plasma mass spectroscopy (ICP-MS). The analysis revealed that the Zn and Mn contents in 30-ZnMn-NC were 1.99 and 1.09 wt %, respectively (Table S1). The N_2 adsorption−desorption isotherm of 30-ZnMn-NC displayed a reversible type IV curve with obvious hysteresis loops (Figures 2e and S5), suggesting a mesoporous structure with an average pore size of 4.9 nm in the composite. This is significantly higher than the pore sizes of 1.8 and 0.9 nm in 10-ZnMn-NC and 50-ZnMn-NC, respectively. The high porosity of 30-ZnMn-NC promotes mass transfer and exposes numerous active sites, facilitating substance transport, endowing the catalyst with faster reaction kinetics in the ORR process. These findings align with prior

https://doi.org/10.1021/acs.inorgchem.3c01536
Inorg. Chem. 2023, 62, 13284−13292

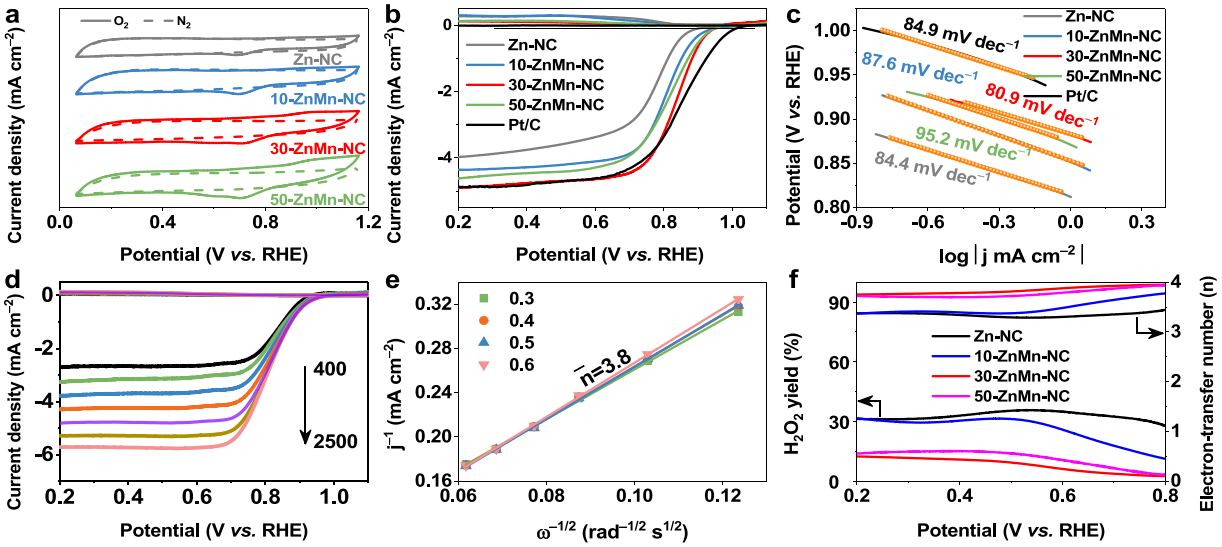

Figure 4. (a) CV curves in N_2/O_2-saturated 0.1 M KOH. (b) LSV polarization curves in O_2-saturated 0.1 M KOH and (c) Tafel plots of different catalysts. (d) Polarization curves of 30-ZnMn-NC measured at different rotating speeds ranging from 400 to 2500 rpm. (e) Corresponding K−L plots. (f) H_2O_2 yield (%) and electron transfer number (n) from various catalysts.

studies, indicating that mesoporous catalysts featuring high porosity and large pore sizes exhibit superior ORR activity.[32] The formation of the porous structure in 30-ZnMn-NC was attributed to the evaporation of Zn atoms at high temperatures.[33] Additionally, the Brunauer−Emmett−Teller (BET) specific surface area of 30-ZnMn-NC was calculated to be 421.7 $m^2\ g^{-1}$, which is slightly lower than the BET specific surface areas of 10-ZnMn-NC (851.2 $m^2\ g^{-1}$) and 50-ZnMn-NC (427.0 $m^2\ g^{-1}$). However, the high utilization rate of the active sites in 30-ZnMn-NC suggests that the smaller BET specific surface area is not a major limitation to its ORR activity.

X-ray Photoelectron Spectroscopy Analysis. XPS analysis was conducted to investigate the surface composition and chemical state of the catalyst. Figure S6a displays the XPS survey spectrum, indicating the presence of C, O, N, Mn, and Zn elements. The high-resolution C 1s spectra of Zn-NC and 30-ZnMn-NC show four peaks (Figure S6b,c), which served as calibration standards for the high-resolution spectra of other elements.[34] The high-resolution Zn 2p spectra of Zn-NC and 30-ZnMn-NC exhibit two main peaks at 1021.2 and 1044.3 eV, attributed to $2p_{3/2}$ and $2p_{1/2}$ of Zn^{2+} (Figure 3a).[35,36] The high-resolution Mn 2p spectrum of 30-ZnMn-NC displays two peaks at 641.1 and 653.4 eV, corresponding to Mn $2p_{3/2}$ and Mn $2p_{1/2}$ of Mn^{2+}, and additional peaks at 645.1 and 657.6 eV, which are attributed to Mn $2p_{3/2}$ and Mn $2p_{1/2}$ of Mn^{3+} (Figure 3b).[37,38] These results confirm that the Mn−N bond is formed after the incorporation of Mn. In addition, the XPS spectra of 10-ZnMn-NC and 50-ZnMn-NC also exhibited similar peaks. N 1s spectrum (Figure 3c) exhibits three prominent peaks at 397.9, 400.2, and 402.9 eV, corresponding to pyridine-N, pyrrole-N, and graphite-N, respectively. Pyrroline-N can act as an electron donor, increasing the electron density of the material and promoting the formation of *OOH. Pyridine-N can coordinate well with the d orbitals of transition metals, making it a preferred site for capturing and anchoring metal atoms.[39] Additionally, as an electron-withdrawing group, the presence of pyridine N in the catalyst aids in reducing the electron density of neighboring carbon atoms, thereby promoting the faster adsorption of intermediates (*OH and *OOH).[40] Notably, the combined content of pyridine and pyrrole N in 30-ZnMn-NC is significantly higher than that in Zn-NC, 10-ZnMn-NC, and 50-ZnMn-NC (Figure S7). This suggests that the appropriate amount of Mn doping promotes the coordination of Mn with pyridine-N/pyrrole-N,[41] thereby enhancing the catalytic activity of the ORR.

Electrocatalytic ORR in Alkaline Electrolytes. The impact of temperature on the catalytic performance of 30-ZnMn-NC was investigated by subjecting it to varying pyrolysis conditions (800, 900, and 1000 °C). As observed in Figure S8, the catalyst demonstrated optimal oxygen reduction potential, half-wave potential, limiting current density, and Tafel slope at a pyrolysis temperature of 900 °C. Figure 4a reveals that the cyclic voltammetry (CV) curves obtained in the O_2-saturated electrolyte display a distinct reduction peak, indicating its superior ORR activity. Additionally, 30-ZnMn-NC provided a more positive reduction peak than the other comparison samples, suggesting its superior ORR activity. Precisely, the E_{onset} (0.95 V) and $E_{1/2}$ (0.83 V) values of 30-ZnMn-NC were proved in Figure 4b, which are superior to those of Zn-NC (0.89 V and 0.76 V), 10-ZnMn-NC (0.94 and 0.80 V), and 50-ZnMn-NC (0.94 V and 0.81 V). Furthermore, these values also outperform the recently reported transition-metal-based electrocatalysts (Figure S9 and Tables S2−3). However, the $E_{1/2}$ value of 30-ZnMn-NC is lower than that of Pt/C (1.01, 0.85 V), which may be due to the different preparation conditions and structural features of the two catalysts. 30-ZnMn-NC is synthesized using a hydrothermal method, while Pt/C is typically made by electrochemical deposition. However, the ORR performance of 30-ZnMn-NC is more attractive than the other comparative samples considering non-noble metal catalysts. This suggests that 30-ZnMn-NC is a promising low-cost catalyst for ORR applications. The exceptional activity of 30-ZnMn-NC can be ascribed to its mesoporous structure, which promotes the diffusion of electrolytes and gases, endowing the catalyst with faster reaction kinetics.[42] As depicted in Figure 4c, the Tafel slope of 30-ZnMn-NC is 80.90 mV dec^{-1}, lower than that of Zn-NC (84.4 mV dec^{-1}), 10-ZnMn-NC (95.2 mV dec^{-1}), 50-ZnMn-NC (87.6 mV dec^{-1}), and the benchmark Pt/C (84.9

https://doi.org/10.1021/acs.inorgchem.3c01536
Inorg. Chem. 2023, 62, 13284−13292

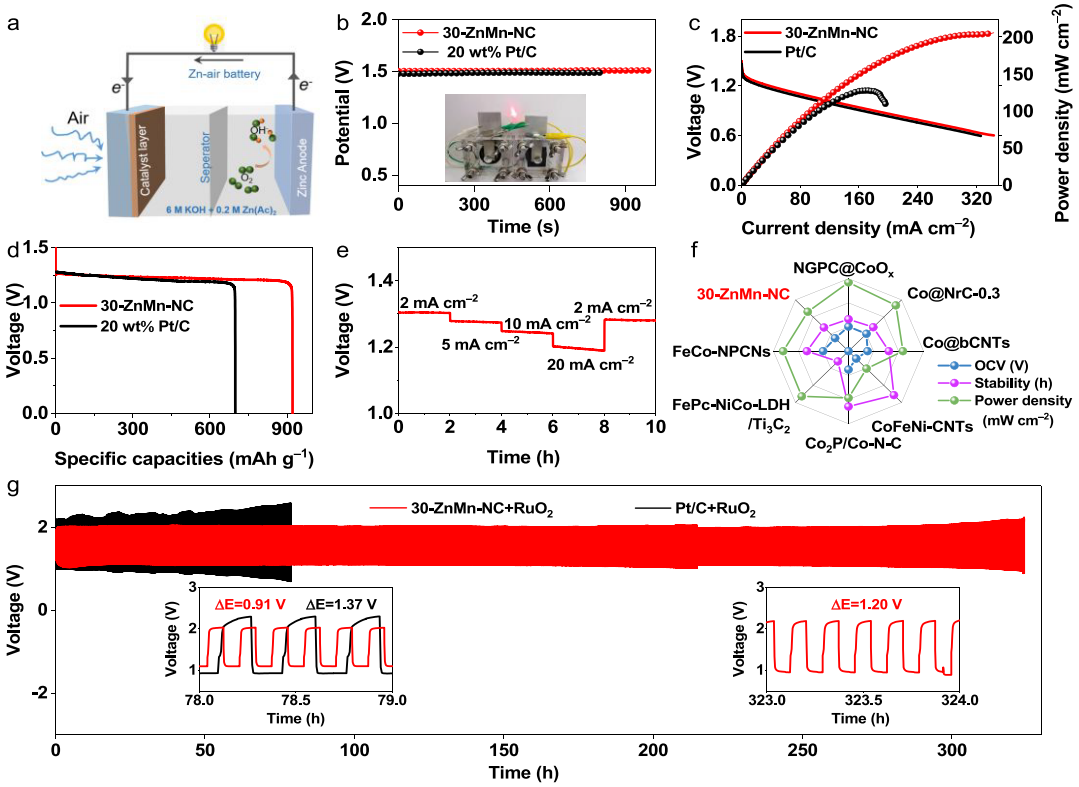

Figure 5. (a) Diagram of the assembled ZAB with 30-ZnMn-NC and Pt/C (20 wt %) as the air cathodes. (b) Open-circuit voltage (OCV) (inset: the LED panel illuminated by two series-connected ZABs). (c) Discharge polarization curves and power densities of the ZABs. (d) Specific capacity plots. (e) Discharge curves at various current densities. (f) Comparison of OCV, stability, and power density between 30-ZnMn-NC-based ZAB and other ZABs reported recently. (g) Galvanostatic cycling at 5 mA cm^{-2}, with each cycle lasting 20 min.

mV dec^{-1}). The lower Tafel slope implies more efficient kinetics in the electrocatalytic process.[43,44] Taken together, these results suggest that the incorporation of an appropriate amount of Mn elements contributes to the catalytic activity of the material. Moreover, the current density of the catalyst exhibits an increase with a higher rotational speed, manifesting different mass transfer rates at different rotational speeds (Figure 4d). The Koutechy−Levich (K−L) diagram also reveals a good linear relationship between $\omega^{-1/2}$ and j^{-1}, evidencing that the electrochemical process follows first-order kinetics.[45] The electron transfer number (n) obtained from the K−L equation calculation is approximately 3.8 (Figure 4e), confirming that the ORR process follows a four-electron transfer path.[46] Furthermore, the selectivity of the product during the electrochemical process was examined in more detail by means of RRDE measurement. Figure 4f demonstrates that the yield of H_2O_2 for 30-ZnMn-NC is approximately 20% with the highest electron transfer number (~3.8) within the potential range of 0.2 ~ 0.8 V (vs RHE), thereby providing further evidence that O_2 is mainly reduced to H_2O through a four-electron pathway during ORR. To assess the electrochemical surface area (ECSA) of the various catalysts and reveal the intrinsic ORR catalyst activity, CV curves (Figure S10) were recorded in the non-Faradaic region at different scan rates to measure the electrochemical double layer capacitance (C_{dl}), as shown in Figure S11.[47] The C_{dl} value of 30-ZnMn-NC is found to be 28.3 mF cm^{-2}, significantly higher than that of Zn-NC (23.6 mF cm^{-2}), 10-ZnMn-NC (28.0 mF cm^{-2}), and 50-ZnMn-NC (27.5 mF cm^{-2}), due to the porous structure of the composite that promotes an increased contact between the reactants and active sites, resulting in an enhanced ORR activity. The ECSA was determined by calculating C_{dl}. This result provided insights into the intrinsic activity of the catalyst. 30-ZnMn-NC exhibited a larger ECSA, implying more available active sites (Figure S12). Methanol tolerance and stability are the critical factors for evaluating the practical feasibility of catalysts.[48] As shown in Figure S13, chronoamperometric response test was conducted in O_2-saturated 0.1 M KOH solution at 1600 rpm. The current density decay rate of 30-ZnMn-NC was only 13% after about 40,000 s of chronoamperometry response, while that of Pt/C was as high as 44%. This demonstrates that 30-ZnMn-NC exhibits satisfactory stability. Furthermore, the current density of Pt/C decreased significantly upon the injection of methanol, whereas the current density of 30-ZnMn-NC remained 88% of the initial value after a sudden change, evidencing its remarkable methanol resistance. This is mainly attributed to its porous structure and cake-like carbon framework, which aid in substance transport and effectively prevent metal ion aggregation during the electrochemical process, respectively. Collectively, these results demonstrate the tremendous potential of 30-ZnMn-NC electrocatalysts for practical applications.

Test for the Performance of Assembled Zinc−Air Batteries. The suitability of 30-ZnMn-NC as an air cathode for energy storage and conversion devices was evaluated in ZAB, as depicted in Figure 5a. This involved supporting 30-ZnMn-NC on a carbon paper, using a Zn foil as the air anode, and employing a mild electrolyte solution consisting of 6.0 M KOH and 0.2 M $Zn(AC)_2$ as the electrolyte. The ZAB incorporating 30-ZnMn-NC exhibited an open-circuit voltage (OCV) of 1.51 V (Figure 5b), which surpassed the OCV of the

https://doi.org/10.1021/acs.inorgchem.3c01536
Inorg. Chem. 2023, 62, 13284−13292

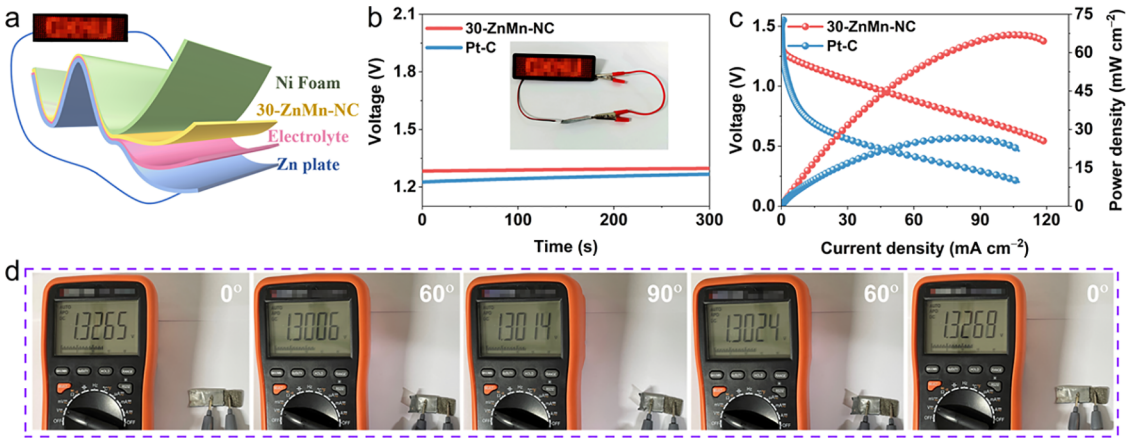

Figure 6. (a) Flexible ZAB assembled with 30-ZnMn-NC/benchmark Pt/C. (b) OCVs of 30-ZnMn-NC- and Pt/C-based flexible ZABs (inset: 30-ZnMn-NC-based flexible ZAB-lit LED board). (c) Discharge polarization and power density of the flexible ZABs. (d) OCVs at different bending angles of 30-ZnMn-NC-based flexible ZAB.

commercial Pt/C (1.48 V). A practical demonstration showed that two ZABs connected in series could power a red LED with a voltage of approximately 3 V (Figure 5b inset). The discharge polarization curve of the ZAB is presented in Figure 5c, demonstrating that the 30-ZnMn-NC-based ZAB achieved a peak power density of 207 mW cm^{-2}, which was considerably higher than that of commercial Pt/C (128 mW cm^{-2}). Moreover, utilizing 30-ZnMn-NC as the air electrode resulted in a remarkably high specific capacity of 922 mA h g_{Zn}^{-1} (Figure 5d), which significantly exceeds that of Pt/C (698 mA h g_{Zn}^{-1}). The discharge curves of the 30-ZnMn-NC-based ZAB at different current densities (2, 5, 10, and 20 mA cm^{-2}) are presented in Figure 5e, which reveal an exceptional rate performance with a voltage loss rate of only 1.5% when the current density was reduced back to 2 mA cm^{-2} after a certain period of time.[49] Figure 5f compares the performance of 30-ZnMn-NC with other recently reported transition-metal-based electrocatalysts in ZAB, demonstrating its immense potential for practical implementation in energy storage−conversion devices.[50,51] In addition, a charge−discharge cycle test was performed at a current density of 5 mA cm^{-2} to evaluate the stability and practical application ability of ZAB. The 30-ZnMn-NC + RuO_2-based ZAB displayed only a small loss of voltage difference after 325 h of continuous charge−discharge (Figure 5g). In contrast, the ZAB assembled with Pt/C + RuO_2 exhibited a notable degradation after 79 h, further confirming that 30-ZnMn-NC possesses extraordinary intrinsic catalytic activity and stability, resulting in a ZAB with exceptional round-trip efficiency, and maintains a stable long-term cycle life.

To investigate its application, the promising ORR activity of 30-ZnMn-NC was integrated into a solid ZAB. In the solid ZAB configuration, the composite is coated on a carbon cloth substrate as the air cathode, while the anode consists of zinc foil, and polyvinyl alcohol (PVA) hydrogel as the solid electrolyte (Figure 6a). According to Figure 6b, the assembled 30-ZnMn-NC-based flexible ZAB yielded a higher OCV of 1.30 V, exceeding that of the Pt/C-based ZAB (1.23 V). The strong discharge capability of the 30-ZnMn-NC-based flexible ZAB was demonstrated by its ability to light up an LED board. The polarization and power density curves presented in Figure 6c demonstrate that the flexible ZAB utilizing 30-ZnMn-NC featured a maximum power density of up to 66.3 mW cm^{-2}, which was significantly higher than that of the Pt/C-based ZAB (26.7 mW cm^{-2}). Moreover, the flexibility and stability of the flexible battery were assessed by measuring the OCVs at various bending angles (0°, 60°, 90°, and returning to 60° and 0°), as demonstrated in Figure 6d. The 30-ZnMn-NC-based ZAB exhibited a high OCV (~1.30 V) and maintained a stable voltage even at different bending angles, indicating excellent stability and flexibility.[52] These results suggest that 30-ZnMn-NC has promising potential and is compared favorably to the catalysts reported in recent studies (Table S4).

Catalytic Mechanism Analysis. As discussed earlier, the 30-ZnMn-NC catalyst demonstrated superior electrocatalytic activity for ORR compared to all other tested catalysts. This was mainly attributed to the following unique merits. First, the increased specific surface area of 30-ZnMn-NC played a crucial role in enhancing the exposure of active sites, resulting in an improved contact between reactants and active sites.[53,54] Second, adjacent metals on N-doped carbon substrates typically transfer electrons to the support, which helps to improve the catalyst's Fermi level and optimize the reaction energy barrier.[55] Lastly, the bimetallic Mn/Zn-N active sites generated by appropriate Mn element doping played a crucial role in synergistically enhancing the ORR activity.[56] These advantages suggest that 30-ZnMn-NC has a promising application in practical energy devices.

CONCLUSIONS

To summarize, ZnMn-NC electrocatalysts with a porous cake-like structure for ORR were prepared *via* a high-temperature pyrolysis strategy. Among all the prepared catalysts, 30-ZnMn-NC exhibited pre-eminent electrocatalytic ORR activity, methanol tolerance, and stability, comparable to the benchmark Pt/C. The mesoporous structure of 30-ZnMn-NC played a significant role in promoting the transport efficiency and imparting the catalyst with fast reaction kinetics. Moreover, the incorporation of N and an appropriate amount of Mn contributed to increasing the active sites, while the synergistic catalytic interaction between the bimetallic components markedly enhanced the ORR activity. Notably, the ZAB constructed using 30-ZnMn-NC achieved an impressive peak power density as high as 207 mW cm^{-2} and a specific capacity of 922 mA h g_{Zn}^{-1}. This work provides a novel strategy for the design and preparation of cost-effective porous non-noble

https://doi.org/10.1021/acs.inorgchem.3c01536
Inorg. Chem. 2023, 62, 13284−13292

metal ORR catalysts with a potential for practical applications in energy devices.

■ ASSOCIATED CONTENT

Supporting Information

The Supporting Information is available free of charge at https://pubs.acs.org/doi/10.1021/acs.inorgchem.3c01536.

Additional experimental details, including methods for material characterization, electrochemical measurements, ECSA calculation, study of ZABs, and ORR comparison data (PDF)

■ AUTHOR INFORMATION

Corresponding Authors

Lei Wang − *Department of Food and Environmental Engineering, Chuzhou Polytechnic, Chuzhou 239000, China*; Email: stone@vip.qq.com

Tayirjan Taylor Isimjan − *Saudi Arabia Basic Industries Corporation (SABIC) at King Abdullah University of Science and Technology (KAUST), Thuwal 23955-6900, Saudi Arabia*; Email: isimjant@sabic.com

Xiulin Yang − *Guangxi Key Laboratory of Low Carbon Energy Materials School of Chemistry and Pharmaceutical Sciences, Guangxi Normal University, Guilin 541004, China*; orcid.org/0000-0003-2642-4963; Email: xlyang@gxnu.edu.cn

Authors

Lixia Wang − *Guangxi Key Laboratory of Low Carbon Energy Materials School of Chemistry and Pharmaceutical Sciences, Guangxi Normal University, Guilin 541004, China*

Meijiao Xu − *Guangxi Key Laboratory of Low Carbon Energy Materials School of Chemistry and Pharmaceutical Sciences, Guangxi Normal University, Guilin 541004, China*

Huatong Li − *Guangxi Key Laboratory of Low Carbon Energy Materials School of Chemistry and Pharmaceutical Sciences, Guangxi Normal University, Guilin 541004, China*

Zhiyang Huang − *Guangxi Key Laboratory of Low Carbon Energy Materials School of Chemistry and Pharmaceutical Sciences, Guangxi Normal University, Guilin 541004, China*

Complete contact information is available at: https://pubs.acs.org/10.1021/acs.inorgchem.3c01536

Author Contributions

The manuscript was written through contributions of all authors. All authors have given approval to the final version of the manuscript. L.W. and M.X. contributed equally to this work.

Notes

The authors declare no competing financial interest.

■ ACKNOWLEDGMENTS

This work was supported by the National Natural Science Foundation of China (no. 21965005), Natural Science Foundation of Guangxi Province (2021GXNSFAA076001), Natural Science Foundation of Education Department of Anhui Province (KJ2021A1406), and Guangxi Technology Base and Talent Subject (GUIKE AD18126001, GUIKE AD20297039).

■ REFERENCES

(1) Song, J.; Yu, D.; Wu, X.; Xie, D.; Sun, Y.; Vishniakov, P.; Hu, F.; Li, L.; Li, C.; Maximov, M. Y.; El-Khatib, K. M.; Peng, S. Interfacial coupling porous cobalt nitride nanosheets array with N-doped carbon as robust trifunctional electrocatalysts for water splitting and Zn-air battery. *Chem. Eng. J.* **2022**, *437*, No. 135281.

(2) Zhao, C. X.; Liu, J. N.; Yao, N.; Wang, J.; Ren, D.; Chen, X.; Li, B. Q.; Zhang, Q. Can Aqueous Zinc-Air Batteries Work at Sub-Zero Temperatures. *Angew. Chem., Int. Ed.* **2021**, *60*, 15281−15285.

(3) Wang, B.; Tang, J.; Zhang, X.; Hong, M.; Yang, H.; Guo, X.; Xue, S.; Du, C.; Liu, Z.; Chen, J. Nitrogen doped porous carbon polyhedral supported Fe and Ni dual-metal single-atomic catalysts: template-free and metal ligand-free sysnthesis with microwave-assistance and d-band center modulating for boosted ORR catalysis in zinc-air batteries. *Chem. Eng. J.* **2022**, *437*, No. 135295.

(4) Cheng, F.; Chen, J. Metal-air batteries: from oxygen reduction electrochemistry to cathode catalysts. *Chem. Soc. Rev.* **2012**, *41*, 2172−2192.

(5) Liu, Y.; Zhang, J.; Li, Y.; Qian, Q.; Li, Z.; Zhang, G. Realizing the Synergy of Interface Engineering and Chemical Substitution for Ni_3N Enables its Bifunctionality Toward Hydrazine Oxidation Assisted Energy-Saving Hydrogen Production. *Adv. Funct. Mater.* **2021**, *31*, No. 2103673.

(6) Zhu, J.; Mu, S. Active site engineering of atomically dispersed transition metal−heteroatom−carbon catalysts for oxygen reduction. *Chem. Commun.* **2021**, *57*, 7869−7881.

(7) Chen, Y.; Ding, R.; Li, J.; Liu, J. Highly active atomically dispersed platinum-based electrocatalyst for hydrogen evolution reaction achieved by defect anchoring strategy. *Appl. Catal., B* **2022**, *301*, No. 120830.

(8) Yang, G.; Zhu, J.; Yuan, P.; Hu, Y.; Qu, G.; Lu, B.-A.; Xue, X.; Yin, H.; Cheng, W.; Cheng, J.; Xu, W.; Li, J.; Hu, J.; Mu, S.; Zhang, J.-N. Regulating Fe-spin state by atomically dispersed Mn-N in Fe-N-C catalysts with high oxygen reduction activity. *Nat. Commun.* **2021**, *12*, 1734.

(9) Yu, S.; Wu, Y.; Xue, Q.; Zhu, J.-J.; Zhou, Y. A novel multi-walled carbon nanotube-coupled CoNi MOF composite enhances the oxygen evolution reaction through synergistic effects. *J. Mater. Chem. A* **2022**, *10*, 4936−4943.

(10) Hu, C.; Liang, Q.; Yang, Y.; Peng, Q.; Luo, Z.; Dong, J.; Isimjan, T. T.; Yang, X. Conductivity-enhanced porous N/P co-doped metal-free carbon significantly enhances oxygen reduction kinetics for aqueous/flexible zinc-air batteries. *J. Colloid Interface Sci.* **2023**, *633*, 500−510.

(11) Liu, B.; Shioyama, H.; Jiang, H.; Zhang, X.; Xu, Q. Metal−organic framework (MOF) as a template for syntheses of nanoporous carbons as electrode materials for supercapacitor. *Carbon* **2010**, *48*, 456−463.

(12) Zhong, H. X.; Wang, J.; Zhang, Y. W.; Xu, W. L.; Xing, W.; Xu, D.; Zhang, Y. F.; Zhang, X. B. ZIF-8 derived graphene-based nitrogen-doped porous carbon sheets as highly efficient and durable oxygen reduction electrocatalysts. *Angew. Chem., Int. Ed.* **2014**, *53*, 14235−14239.

(13) Ge, L.; Yang, Y.; Wang, L.; Zhou, W.; De Marco, R.; Chen, Z.; Zou, J.; Zhu, Z. High activity electrocatalysts from metal−organic framework-carbon nanotube templates for the oxygen reduction reaction. *Carbon* **2015**, *82*, 417−424.

(14) Zhong, Y.; Xia, X.; Shi, F.; Zhan, J.; Tu, J.; Fan, H. J. Transition Metal Carbides and Nitrides in Energy Storage and Conversion. *Adv. Sci.* **2016**, *3*, No. 1500286.

(15) Li, J. C.; Hou, P. X.; Liu, C. Heteroatom-Doped Carbon Nanotube and Graphene-Based Electrocatalysts for Oxygen Reduction Reaction. *Small* **2017**, *13*, No. 201702002.

(16) Liu, H.; Lei, J.; Yang, S.; Qin, F.; Cui, L.; Kong, Y.; Zheng, X.; Duan, T.; Zhu, W.; He, R. Boosting the oxygen evolution activity over cobalt nitride nanosheets through optimizing the electronic configuration. *Appl. Catal., B* **2021**, *286*, No. 119894.

(17) Li, W.; Jiang, Y.; Li, Y.; Gao, Q.; Shen, W.; Jiang, Y.; He, R.; Li, M. Electronic modulation of CoP nanoarrays by Cr-doping for efficient overall water splitting. *Chem. Eng. J.* **2021**, *425*, No. 130651.
(18) Ratso, S.; Kruusenberg, I.; Kärik, M.; Kook, M.; Saar, R.; Kanninen, P.; Kallio, T.; Leis, J.; Tammeveski, K. Transition metal-nitrogen co-doped carbide-derived carbon catalysts for oxygen reduction reaction in alkaline direct methanol fuel cell. *Appl. Catal., B* **2017**, *219*, 276−286.
(19) Chen, S.; Zhang, N.; Narváez Villarrubia, C. W.; Huang, X.; Xie, L.; Wang, X.; Kong, X.; Xu, H.; Wu, G.; Zeng, J.; Wang, H.-L. Single Fe atoms anchored by short-range ordered nanographene boost oxygen reduction reaction in acidic media. *Nano Energy* **2019**, *66*, No. 104164.
(20) Xu, Z.; Zhu, J.; Shao, J.; Xia, Y.; Tseng, J.; Jiao, C.; Ren, G.; Liu, P.; Li, G.; Chen, R.; Chen, S.; Huang, F.; Wang, H.-L. Atomically dispersed cobalt in core-shell carbon nanofiber membranes as super-flexible freestanding air-electrodes for wearable Zn-air batteries. *Energy Storage Mater.* **2022**, *47*, 365−375.
(21) Gong, L.; Zhu, J.; Xia, F.; Zhang, Y.; Shi, W.; Chen, L.; Yu, J.; Wu, J.; Mu, S. Marriage of Ultralow Platinum and Single-Atom MnN_4 Moiety for Augmented ORR and HER Catalysis. *ACS Catal.* **2023**, *13*, 4012−4020.
(22) Liu, K.; Qiao, Z.; Hwang, S.; Liu, Z.; Zhang, H.; Su, D.; Xu, H.; Wu, G.; Wang, G. Mn- and N-doped carbon as promising catalysts for oxygen reduction reaction: Theoretical prediction and experimental validation. *Appl. Catal., B* **2019**, *243*, 195−203.
(23) Xiong, X.; Li, Y.; Jia, Y.; Meng, Y.; Sun, K.; Zheng, L.; Zhang, G.; Li, Y.; Sun, X. Ultrathin atomic Mn-decorated formamide-converted N-doped carbon for efficient oxygen reduction reaction. *Nanoscale* **2019**, *11*, 15900−15906.
(24) Wu, F.; Feng, B.; Li, W.; Liu, H.; Mei, Y.; Hu, W. Efficient oxygen reduction electrocatalysis on Mn_3O_4 nanoparticles decorated N-doped carbon with hierarchical porosity and abundant active sites. *Int. J. Hydrogen Energy* **2019**, *44*, 26387−26395.
(25) Dessie, Y.; Tadesse, S.; Eswaramoorthy, R.; Abebe, B. Recent developments in manganese oxide based nanomaterials with oxygen reduction reaction functionalities for energy conversion and storage applications: A review. *J. Sci.: Adv. Mater. Devices* **2019**, *4*, 353−369.
(26) Nivedha, L. K.; Murugaiah, D. K.; Kandregula, G. R.; Murugan, R.; Ramanujam, K. $ZnMn_2O_4$/Carbon Composite Recycled from Spent Zinc-Carbon Batteries for Zn-Air Battery Applications. *J. Electrochem. Soc.* **2022**, *169*, 100544.
(27) Qian, M.; Guo, M.; Qu, Y.; Xu, M.; Liu, D.; Hou, C.; Isimjan, T. T.; Yang, X. Energy barrier engineering of oxygen reduction reaction synergistically promoted by binary Zn-Cu pair sites for advanced Zn−air batteries. *J. Alloys Compd.* **2022**, *907*, No. 164527.
(28) Tang, Y.-J.; You, L.; Zhou, K. Enhanced Oxygen Evolution Reaction Activity of a Co_2P@NC−Fe_2P Composite Boosted by Interfaces Between a N-Doped Carbon Matrix and Fe_2P Microspheres. *ACS Appl. Mater. Interfaces* **2020**, *12*, 25884−25894.
(29) Li, T.; Hu, Y.; Liu, K.; Yin, J.; Li, Y.; Fu, G.; Zhang, Y.; Tang, Y. Hollow yolk-shell nanoboxes assembled by Fe-doped Mn_3O_4 nanosheets for high-efficiency electrocatalytic oxygen reduction in Zn-Air battery. *Chem. Eng. J.* **2022**, *427*, No. 131992.
(30) Ruan, Q.-D.; Feng, R.; Feng, J.-J.; Gao, Y.-J.; Zhang, L.; Wang, A.-J. High-Activity Fe_3C as pH-Universal Electrocatalyst for Boosting Oxygen Reduction Reaction and Zinc-Air Battery. *Small* **2023**, *19*, No. 2300136.
(31) Niu, W.-J.; Yan, Y.-Y.; Li, R.-J.; Zhao, W.-W.; Chen, J.-L.; Liu, M.-J.; Gu, B.; Liu, W.-W.; Chueh, Y.-L. Identifying the impact of Fe nanoparticles encapsulated by nitrogen-doped carbon to Fe single atom sites for boosting oxygen reduction reaction toward Zn-air batteries. *Chem. Eng. J.* **2023**, *456*, No. 140858.
(32) Zhu, Q.-L.; Xia, W.; Zheng, L.-R.; Zou, R.; Liu, Z.; Xu, Q. Atomically Dispersed Fe/N-Doped Hierarchical Carbon Architectures Derived from a Metal−Organic Framework Composite for Extremely Efficient Electrocatalysis. *ACS Energy Lett.* **2017**, *2*, 504−511.
(33) Chen, X.; Shen, K.; Chen, J.; Huang, B.; Ding, D.; Zhang, L.; Li, Y. Rational design of hollow N/Co-doped carbon spheres from bimetal-ZIFs for high-efficiency electrocatalysis. *Chem. Eng. J.* **2017**, *330*, 736−745.
(34) Yang, Y.; Dai, Q.; Shi, L.; Liu, Y.; Isimjan, T. T.; Yang, X. Electronic Modulation of Pt Nanoparticles on Ni_3N−Mo_2C by Support-Induced Strategy for Accelerating Hydrogen Oxidation and Evolution. *J. Phys. Chem. Lett.* **2022**, *13*, 2107−2116.
(35) Tong, M.; Sun, F.; Xie, Y.; Wang, Y.; Yang, Y.; Tian, C.; Wang, L.; Fu, H. Operando Cooperated Catalytic Mechanism of Atomically Dispersed Cu-N_4 and Zn-N_4 for Promoting Oxygen Reduction Reaction. *Angew. Chem., Int. Ed.* **2021**, *60*, 14005−14012.
(36) Wang, J.; Li, H.; Liu, S.; Hu, Y.; Zhang, J.; Xia, M.; Hou, Y.; Tse, J.; Zhang, J.; Zhao, Y. Turning on Zn 4s Electrons in a N_2-Zn-B_2 Configuration to Stimulate Remarkable ORR Performance. *Angew. Chem., Int. Ed.* **2021**, *60*, 181−185.
(37) Tong, J.; Wang, H.; Bo, L.; Li, C.; Guan, X.; Kong, D.; Zhang, Y.; Shi, W.; Lei, Z. Mn-doped Co_2P/N-doped carbon composite materials as efficient bifunctional catalysts for rechargeable Zn-air batteries. *Mater. Res. Bull.* **2022**, *147*, No. 111638.
(38) Zhou, X.; Xu, D.; Chen, Y.; Hu, Y. Enhanced degradation of triclosan in heterogeneous E-Fenton process with MOF-derived hierarchical Mn/Fe@PC modified cathode. *Chem. Eng. J.* **2020**, *384*, No. 123324.
(39) Wang, H.; Wei, L.; Liu, J.; Shen, J. Hollow bimetal ZIFs derived Cu/Co/N co-coordinated ORR electrocatalyst for microbial fuel cells. *Int. J. Hydrogen Energy* **2020**, *45*, 4481−4489.
(40) Li, F.; Qin, T.; Sun, Y.; Jiang, R.; Yuan, J.; Liu, X.; O'Mullane, A. P. Preparation of a one-dimensional hierarchical MnO@CNT@Co−N/C ternary nanostructure as a high-performance bifunctional electrocatalyst for rechargeable Zn−air batteries. *J. Mater. Chem. A* **2021**, *9*, 22533−22543.
(41) Zheng, W.; Chen, F.; Zeng, Q.; Li, Z.; Yang, B.; Lei, L.; Zhang, Q.; He, F.; Wu, X.; Hou, Y. A Universal Principle to Accurately Synthesize Atomically Dispersed Metal−N_4 Sites for CO_2 Electroreduction. *Nano-Micro Lett.* **2020**, *12*, 108.
(42) Liu, M.; Wang, L.; Zhang, L.; Zhao, Y.; Chen, K.; Li, Y.; Yang, X.; Zhao, L.; Sun, S.; Zhang, J. In-Situ Silica Xerogel Assisted Facile Synthesis of Fe-N-C Catalysts with Dense Fe-N_x Active Sites for Efficient Oxygen Reduction. *Small* **2022**, *18*, No. 2104934.
(43) Harzandi, A. M.; Shadman, S.; Nissimagoudar, A. S.; Kim, D. Y.; Lim, H.-D.; Lee, J. H.; Kim, M. G.; Jeong, H. Y.; Kim, Y.; Kim, K. S. Ruthenium Core−Shell Engineering with Nickel Single Atoms for Selective Oxygen Evolution via Nondestructive Mechanism. *Adv. Energy Mater.* **2021**, *11*, No. 2003448.
(44) Wang, L.; Huang, M.; Gao, M.; Isimjan, T. T.; Yang, X. Electron-transfer enhancement of urchin-like CoP−$Ce_2(CO_3)_2O$/NF as an ultra-stable bifunctional catalyst for efficient overall water splitting. *Mater. Chem. Front.* **2023**, *7*, 2628−2636.
(45) Lin, S.-Y.; Xia, L.-X.; Cao, Y.; Meng, H.-L.; Zhang, L.; Feng, J.-J.; Zhao, Y.; Wang, A.-J. Electronic Regulation of ZnCo Dual-Atomic Active Sites Entrapped in 1D@2D Hierarchical N-Doped Carbon for Efficient Synergistic Catalysis of Oxygen Reduction in Zn−Air Battery. *Small* **2022**, *18*, No. 2107141.
(46) Shao, X.; Yang, Y.; Liu, Y.; Yan, P.; Zhou, S.; Taylor Isimjan, T.; Yang, X. Oxygen vacancy-rich N-doped carbon encapsulated BiOCl-CNTs heterostructures as robust electrocatalyst synergistically promote oxygen reduction and Zn-air batteries. *J. Colloid Interface Sci.* **2022**, *607*, 826−835.
(47) Liu, J.; Zhou, J.; Leung, M. K. H. Valence Engineering of Polyvalent Cobalt Encapsulated in a Carbon Nanofiber as an Efficient Trifunctional Electrocatalyst for the Zn−Air Battery and Overall Water Splitting. *ACS Appl. Mater. Interfaces* **2022**, *14*, 4399−4408.
(48) Guo, M.; Huang, Z.; Qu, Y.; Wang, L.; Li, H.; Isimjan, T. T.; Yang, X. Synergistic effect and nanostructure engineering of three-dimensionally hollow mesoporous spherical Cu_3P/TiO_2 in aqueous/flexible Zn−air batteries. *Appl. Catal., B* **2023**, *320*, No. 121991.
(49) Guo, M.; Xu, M.; Qu, Y.; Hu, C.; Yan, P.; Isimjan, T. T.; Yang, X. Electronic/mass transport increased hollow porous Cu_3P/MoP

https://doi.org/10.1021/acs.inorgchem.3c01536
Inorg. Chem. 2023, 62, 13284−13292

nanospheres with strong electronic interaction for promoting oxygen reduction in Zn-air batteries. *Appl. Catal., B* **2021**, *297*, No. 120415.
(50) Yu, J.; Dai, Y.; Zhang, Z.; Liu, T.; Zhao, S.; Cheng, C.; Tan, P.; Shao, Z.; Ni, M. Tailoring structural properties of carbon via implanting optimal co nanoparticles in n-rich carbon cages toward high-efficiency oxygen electrocatalysis for rechargeable zn-air batteries. *Carbon Energy* **2022**, *4*, 576−585.
(51) Zhao, Y.; Wang, X.; Guo, X.; Shi, N.; Cheng, D.; Zhou, H.; Saito, N.; Fan, T. Nitrogen-doped 3D porous graphene coupled with densely distributed CoO_x nanoparticles for efficient multifunctional electrocatalysis and Zn-Air battery. *Electrochim. Acta* **2022**, *420*, No. 140432.
(52) Hu, C.; Wei, F.; Liang, Q.; Peng, Q.; Yang, Y.; Taylor Isimjan, T.; Yang, X. Electronically modulated d-band centers of MOF-derived carbon-supported Ru/HfO_2 for oxygen reduction and aqueous/flexible zinc-air batteries. *J. Energy Chem.* **2023**, *80*, 247−255.
(53) Xu, F.; Wang, J.; Zhang, Y.; Wang, W.; Guan, T.; Wang, N.; Li, K. Structure-engineered bifunctional oxygen electrocatalysts with Ni_3S_2 quantum dot embedded S/N-doped carbon nanosheets for rechargeable Zn-air batteries. *Chem. Eng. J.* **2022**, *432*, No. 134256.
(54) Wang, Z.-D.; Liang, S.; Bai, C.-K.; Guo, Z.-F.; Lu, G.-L.; Sun, H.; Liu, Z.-N.; Zang, H.-Y. Synergistically enhanced iron and zinc bimetallic sites as an advanced ORR electrocatalyst for flow liquid rechargeable Zn−air batteries. *J. Mater. Chem. A* **2022**, *10*, 3169−3177.
(55) Jeong, D. I.; Choi, H. W.; Woo, S.; Yoo, J. H.; Kang, D.; Kim, S.; Lim, B.; Kim, J. H.; Kim, S.-W.; Kang, B. K.; Yoon, D. H. Electronic structure modification and N-doped carbon shell nano-architectonics of Ni_3FeN@NC for overall water splitting performance evaluation. *J. Mater. Chem. A* **2022**, *10*, 16704−16713.
(56) Zheng, X.; Cao, Y.; Wang, H.; Zhang, J.; Zhao, M.; Huang, Z.; Wang, Y.; Zhang, L.; Deng, Y.; Hu, W.; Han, X. Designing Breathing Air-electrode and Enhancing the Oxygen Electrocatalysis by Thermo-electric Effect for Efficient Zn-air Batteries. *Angew. Chem., Int. Ed.* **2023**, *62*, No. e202302689.

https://doi.org/10.1021/acs.inorgchem.3c01536
Inorg. Chem. 2023, 62, 13284−13292